The Seismic Record of Wind in Alaska

Cade A. Quigley*1[®] and Michael E. West²

ABSTRACT

Seismic data contains a continuous record of wind influenced by different factors across the frequency spectrum. To assess the influences of wind on ground motion, we use colocated wind and seismic data from 110 stations in the Alaska component of the EarthScope Transportable Array. We compare seismic probability power spectral densities and wind speed and direction during 2018 to develop a quantitative measure of the seismic sensitivity to wind. We observe a pronounced increase in seismic energy as a function of wind speed for almost all stations. At frequencies below the microseism band, our observations agree with previous authors in finding that sensor emplacement and ground materials are important, and that much of the wind influence likely comes from associated changes in barometric pressure. Wind has the least influence in the microseism band, but that is only because its contribution to noise is much smaller than the ubiquitous microseism background. At frequencies above the microseism band, we find that wind sensitivity is correlated with land cover type, increasing with vegetation height. This sensitivity varies seasonally, which we attribute to snow insulation, the burial of vegetation and objects around the station, and potentially the role of frozen ground. Wind direction also manifests in seismic data, which we attribute to turbulent air on the lee side of station huts coupling with the ground and the seismometer borehole cap. We find some dependence on bedrock type, with a greater seismic response in unconsolidated sediment. These results provide guidance on site selection and construction, and make it possible to forecast seismic network performance under different wind conditions. When we examine the factors at work in a warming climate, we find reason to anticipate increasing seismic noise from wind in the Arctic over the decades to come.

KEY POINTS

- Seismic data contain a continuous record of wind, influenced by environmental and local site conditions.
- We find that vegetation, bedrock type, and snow burial determine the sensitivity of seismic data to wind.
- Seismic records in Alaska are likely to become more influenced by wind as the climate warms.

Supplemental Material

INTRODUCTION

Seismic networks, while typically designed to capture discrete events such as earthquakes, record the continuous background din of the Earth, comprising a mix of environmental phenomena and human activity. Wind is one of the most prevalent sources of environmental noise visible across most of the frequency spectrum (Frankinet et al., 2021). Wind can produce ground-motion amplitudes that are similar to or exceed those of small earthquakes (Withers et al., 1996; Johnson et al., 2019). Long-period (40–1000 s) atmosphere-induced seismicity has been studied extensively and is attributed to multiple mechanisms related to atmospheric pressure gravity (e.g., Ziolkowski, 1973; Beauduin et al., 1996; Zürn and Wielandt,

2007; De Angelis and Bodin, 2012; Johnson et al., 2017; Tanimoto and Wang, 2018; Anthony et al., 2022). Higher-frequency wind-induced noise (>1 Hz) has been attributed to shear-stress perturbations caused by wind turbulence on the ground (Yu et al., 2011; Naderyan et al., 2016; Mohammadi et al., 2019), direct interaction with seismic sensors and near-surface structures (Withers et al., 1996; Dybing et al., 2019; Johnson et al., 2019), and possible local brittle failures in the subsurface from the movement of vegetation and structures (Johnson et al., 2019). Wind-generated ground motion has been shown to decrease with depth from the surface (Hutt et al., 2017). For this reason, installation style (i.e., vault, posthole, borehole) and depth of seismometer are important considerations for data quality (Aderhold et al., 2015). Because the amplitude of wind-induced signals is dependent on the amount of kinetic energy transferred into mechanical

Cite this article as Quigley, C. A., and M. E. West (2023). The Seismic Record of Wind in Alaska, Bull. Seismol. Soc. Am. XX, 1-14, doi: 10.1785/0120230097

© Seismological Society of America

^{1.} Department of Geology, Colorado College, Colorado Springs, Colorado, U.S.A., https://orcid.org/0009-0000-3184-8109 (CAQ); 2. Alaska Earthquake Center,

Geophysical Institute, University of Alaska Fairbanks, Fairbanks, Alaska, U.S.A.,

⁽MEW) https://orcid.org/0000-0003-4855-9295

^{*}Corresponding author: c_quigley@coloradocollege.edu

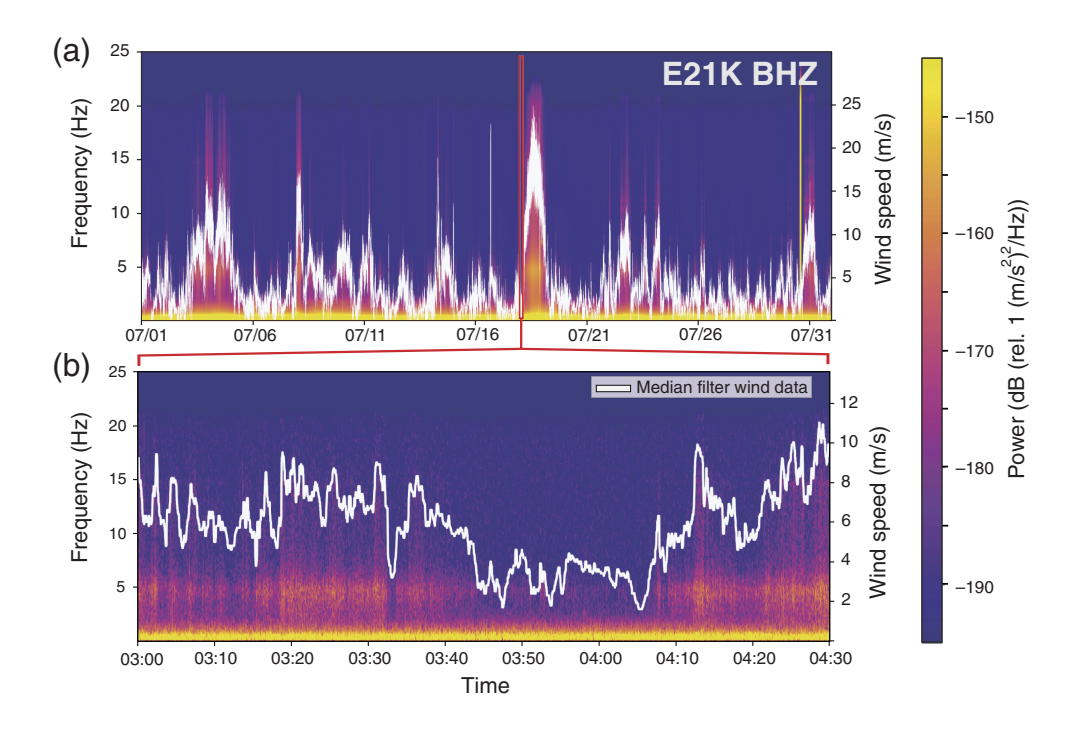


Figure 1. (a) Spectrogram of E21K (channel BHZ) for July 2018. The spectrogram is overlain with median-filtered wind speed data (channel LWS). Large, bright spikes in the seismic and wind data are storms. (b) Ninety minute inset of panel (a) for 18 July 2018. Times are in UTC.

energy (i.e., elastic ground deformation), wind speed, direction, and local topography can all influence the seismic record of wind (Naderyan *et al.*, 2016; Lott *et al.*, 2017; Frankinet *et al.*, 2021).

Wind is evident in the seismic record on all time scales (Fig. 1). On the scale of days to months, seismic power fluctuates

0.1 Hz 0.02 Hz **G29M** band band Power (dB (rel. 1 (m/s²)² /Hz)) -120-140 -160 2 Hz 6 Hz 18 Hz -180band band band 10² 10^{-1} 10⁰ 10¹ Period (s)

Figure 2. Probabilistic power spectral densities (PPSDs) calculated for 10 one hour segments of BHZ data recorded at station G29M in July 2018. The line color indicates average hourly wind speeds. Vertical colored boxes indicated the bounds of the frequency bands investigated, with the center frequency indicated with a solid gray line. Figure follows the style of Frankinet *et al.* (2021).

by tens of decibels in response to storms and diurnal patterns (Fig. 1a; Fyen, 1988). Shorter time scales (seconds minutes) show similar patterns in which changes in wind speed are mirrored instantaneously by changes in seismic energy (Fig. 1b). All authors show significant variability in the style and amplitude of the seismic response to wind, even when seismometers are in close proximity. These differences provide a potentially rich source of information about the surrounding environment and station design.

One approach to quantifying the influence of wind is through probabilistic power spectral density (PPSD; McNamara and Boaz, 2005; Lott *et al.*, 2017; Frankinet *et al.*, 2021). Comparing time averages of

the wind speed to PPSDs allows this relationship to be tracked across time and frequency (Fig. 2). The relationship between wind velocity and seismic energy has been demonstrated as linear (Lott *et al.*, 2017; Dybing *et al.*, 2019; Johnson *et al.*, 2019) and bilinear (Frankinet *et al.*, 2021). Similarly, the slope of the relationship has been shown to change based on the direction of the

wind. This is intuitive and has been attributed to differences in local topography and surface obstacles such as trees and structures (Dybing *et al.*, 2019; Lott *et al.*, 2017; Johnson *et al.*, 2019). Frankinet *et al.* (2021) demonstrate that for some sites, there is a critical wind speed below which wind has only a minimal impact on ground motion.

Our objective is to determine the primary controls on how wind manifests in seismic records, with an emphasis on cold environments and Arctic landscapes. We do this by examining the expansive set of colocated wind and seismic records across Alaska and northwestern Canada from

the EarthScope Transportable Array (TA) deployment. The TA covered nearly two million square kilometers in Alaska, encompassed a huge range in geography and ecology, and was largely free of anthropogenic contamination. We use these data to examine wind and seismic records over the course of a year. We conduct wind–seismic comparisons in five different frequency bands to characterize this influence across the frequency spectrum. The diversity of environmental conditions and station configurations allows quantitative observations that should be portable to other locations, and can be used for advising future seismic deployments and identifying wind effects in seismic data obtained from existing networks.

DATA

During the final stage of the EarthScope USArray Transportable Array program (Meltzer et al., 1999; Busby et al., 2018), 195 new stations were installed across Alaska and western Canada. Together with upgrades at dozens of existing seismic stations, the final composite network achieved a nominal station spacing of 85 km. The grid-like spacing and even sampling across wide geographic regions are hallmarks of the TA project (Long et al., 2014). Following an installation period between 2014 and 2018, the network operated in full into 2020 (Busby and Aderhold, 2020). In 2019 and 2020, a little more than half the new stations were transferred to other networks for long-term operation. The remaining sites were decommissioned in 2020 and 2021. In addition to three component broadband seismometers, 146 TA stations were equipped with Vaisala WXT-520 or WXT-536 weather stations. These weather stations are capable of measuring wind speed and direction, atmospheric pressure, temperature, relative humidity, rain intensity, and hail intensity, all with a sampling rate of 1 sample per second (sps)—a much higher rate than most publicly available weather data. The majority of weather stations are ~3 m above the ground, installed 1.2 m above the top of the station enclosure. The stations used in this study were equipped with either a Streckeisen STS-5A or Nanometrics Trillium 120 s PH seismometer sampling at 40 sps.

The Alaska TA stations cover multiple mountain ranges, border 5 major ocean regions (Bering Sea, Chukchi Sea, Beaufort Sea, North Pacific Ocean, and Gulf of Alaska), and span 32 ecoregions (Nowacki et al., 2003). Stations range in elevation from 5–2600 m and cover eight major land cover zones (Dewitz, 2021). Meteorologically, these regions experience vastly different storm systems. During the installation of the TA, environmental parameters (e.g., vegetation type, material around the borehole, and presence of trees) and station-specific parameters (e.g., installation method, distance to borehole, posthole casing material) were well documented (Table S4, available in the supplemental material to this article; Busby and Aderhold, 2020). These station data, augmented by regional datasets such as the Geologic Map of Alaska (Wilson et al., 2015) and the National Land Cover Database (NLCD)

(Dewitz, 2021), make it possible to explore the controls on wind-induced seismic noise.

WIND SENSITIVITY

To extract environmental and station design influences on the seismic sensitivity to wind, we developed methodologies for systematic comparison through time. We devised an approach that is largely unaffected by the many other sources of seismicity, including earthquakes. The PPSD approach of McNamara and Boaz (2005) provides an excellent way to measure the median seismic energy at specific frequency bands while minimizing the influence of short-lived events. We use hourly PPSDs for 2018—a year that offers the most spatially and temporally complete records. We focus our analysis on vertical component records. At periods above the microseism band, we find similar behavior between the vertical and horizontal channels (Figs. S1-S3). Below the microseism band, the horizontal components show greater overall sensitivity to wind (Figs. S1-S3), in keeping with observations over the past half century that are well summarized in Tanimoto and Wang (2018) and Dybing et al. (2019) and references therein. Because we observe comparable patterns on all components, especially at high frequencies, we focus attention on the vertical ground motions.

Data preparation

The PPSDs for each station are obtained from the Modular Utility for STAtistical kNowledge Gathering (MUSTANG) noise-psd web service through the Incorporated Research Institutions for Seismology (IRIS Transportable Array, 2003; Casey et al., 2018). We then create matching hourly values for the wind data. The 1 Hz wind speed and direction (channels LWS and LWD) contain occasional gaps and unrealistic zero values lasting a few seconds. We find that a 15 s median filter smooths out the vast majority of nonphysical fluctuations (Fig. S4). We calculate the mean of hour-long segments of wind speed. To derive an hourly wind direction, we decompose the 1 Hz wind direction unit vector into north-south and eastwest components. We average these components independently and recombine the component averages to get an overall average direction. Any hours that are missing either wind or seismic data are removed from the dataset. This results in over 900,000 time samples of wind and seismic energy at 96 frequency bands.

The PPSDs used in this study were obtained from the MUSTANG noise-psd web service. The preparation of these records includes steps that smooth the spectra across frequency windows with a width of one octave (Casey et al., 2018). This smoothing removes jitter between adjacent frequencies, highlighting broad patterns in the data. This approach has also been criticized for smearing energy into adjacent frequency bands, at times masking significant features and skewing seismic power estimates (Anthony et al., 2020). This is of particular

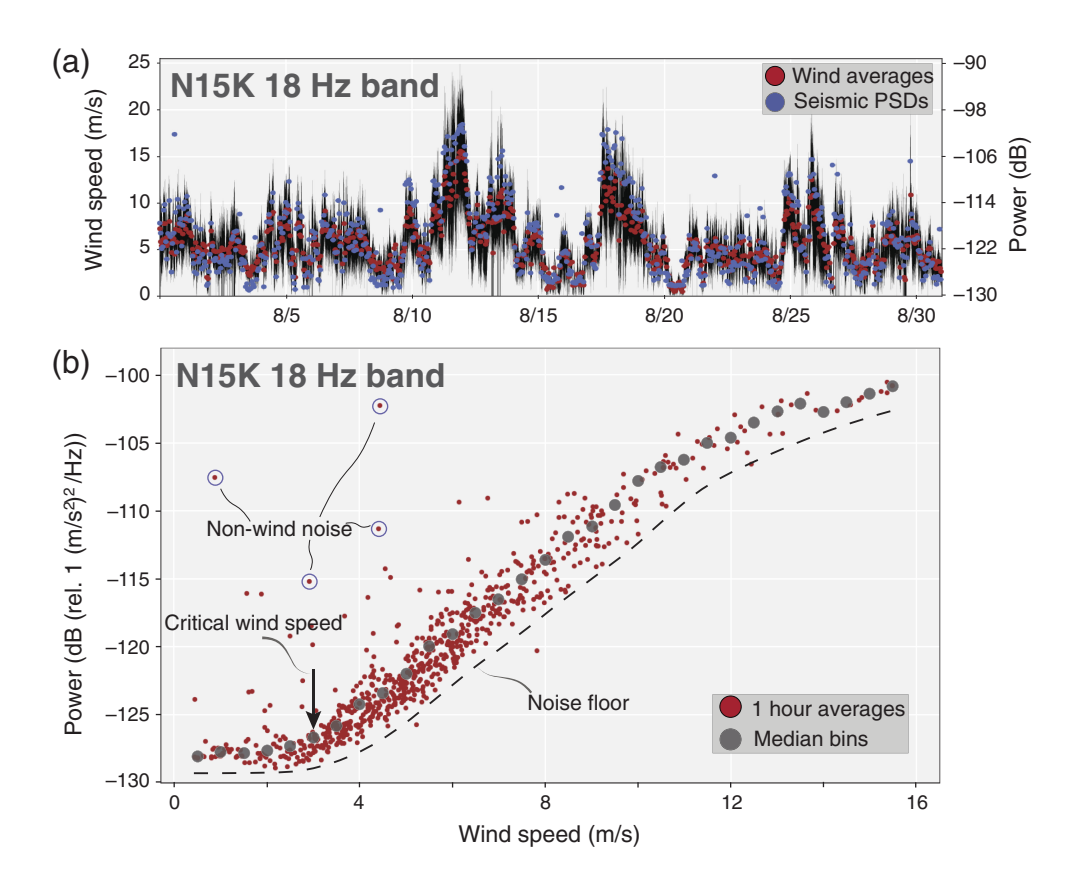


Figure 3. (a) Wind speed for station N15K during August 2018. Red dots are hourly wind speed, and blue dots are hourly seismic PPSDs at 18 Hz. (b) Seismic power as a function of wind speed for August 2018. Gray dots are median power values within 0.5 m/s bins. Values well above the curve originate from non-wind sources. Critical wind speed indicates wind speed at which a significant seismic response occurs.

concern in the \sim 0.5 to 0.05 Hz range, in which the primary and secondary microseism can have sharp peaks closely spaced in frequency.

We leverage the spectral smoothing built into MUSTANG to extract seismic powers averaged across comparably spaced frequency windows. We use values at a specific center frequency, recognizing that they, in fact, represent an octave-wide band. To broadly capture the wind influence in different ranges of interest in seismology, we select bands with five different center frequencies: 0.02 Hz in the range of long-period teleseismic surface waves, 0.1 Hz in the middle of the primary and secondary

microseisms, 2 Hz for regional and teleseismic body waves, 6 Hz for local and regional body waves, and 18 Hz to capture the highest frequencies available in the 40 sps data. Table 1 shows the frequency bands represented by each of these center frequencies.

We recognize that choice to use smoothed frequency spectra may be controversial. We analyzed the impact of using smoothed and unsmoothed spectra for this analysis. For the analysis, as carried out here, we find the two approaches to produce highly correlated (mostly R > 0.97). In a couple of instances, we find a bias of a few dB that is steady over time and an order of magnitude than the smaller wind influences being examined. The supplemental materials contain a thorough side-by-side analysis (Text S1, Table S1 and S2, and Figs. S5-S8).

Methodology

We observe a first-order positive correlation with seismic energy closely following changes in wind speed (Fig. 3). For frequencies ≥1 Hz, the wind–seismic energy curve generally follows a logistic-like curve illustrated in Figure 3b. The total change in power in this example is 27 dB, as wind speed increases from 0 to 15 m/s. There is a clear noise floor at about −129 dB. The data also overrepresent lower wind speeds, indicating the stations are calm (i.e., light breeze) most of the time. When interpreting the data in Figure 3, it is important to keep in mind that these plots reflect the accumulation of all sources of seismic energy, including

TABLE 1		
Frequency	Bands	Investigated

Band Name	Center Frequency (Hz)	Frequency Range (Hz)	Period Range (s)
18 Hz band	18.102	12.80–20	0.05-0.078
6 Hz band	5.868	4.15–8.30	0.121-0.241
2 Hz band	2.075	1.467–2.934	0.341-0.682
0.1 Hz band	0.1	0.071-0.141	7.072-14.144
0.02 Hz band	0.019	0.014–0.027	36.630-73.529

The first column indicates the name we use for each frequency band.

increased seismicity, human activity, and other environmental events. Points from non-wind sources fall above the wind-seismic curve as outliers.

The shape and steepness of these curves are variable. We initially tried to develop an empirical scheme for categorizing stations based on the shape and range of the wind-PPSD curves (Quigley et al., 2021). The disparate set of shapes made it challenging to extract consistent observations. Though this relationship could be captured using higher order polynomials, we struggle to see meaningful and consistent interpretation across a set of polynomial coefficients. The first-order linear relationship, however, is easily interpretable, ubiquitous in the data, and allows for robust comparisons across stations and parameters.

To minimize bias introduced by non-wind noise sources and the low-wind skewness of the dataset, we calculate the median seismic power in each bin of 0.5 m/s (Fig. 3b). This approach works well at frequency bands above 1 Hz, because the number of non-wind outlier data points is generally small. At frequency bands below 1 Hz, there is a substantial amount of non-wind-generated noise. For long-period data, we calculate the 5% percentile of each wind speed bin. The 5% percentile method is stable against points well above the wind-seismic power curve (Lott *et al.*, 2017; Frankinet *et al.*, 2021). When there are relatively few outliers, the median and 5% percentile methods produce similar values for wind sensitivity.

We fit a linear regression to the binned data. The linear regression is described by the following relationship:

$$P = sv + p_0, \tag{1}$$

in which P (dB) is the seismic power in decibels, v (m/s) is the wind speed, p_0 (dB) is the y intercept of power, and s [(dB)/(m/s)] is the slope of the linear regression. p_0 is an approximation for the seismic power at a station when the wind velocity v=0 m/s. The value p_0 is consistently an underestimate of the background seismic noise because most of the curves flatten as they approach zero wind speed, so it should not be considered the true noise floor. Slope s reflects how sensitive a station is to wind-induced ground motion. We refer to this value as the *wind sensitivity*. Lott et al. (2017) refer to a similar measure as ground-motion susceptibility.

Binning the median and 5% percentile seismic energy is effective at capturing the wind speed and seismic power relationship when there are many points; however, the method can fail when there are limited data points. This is problematic for higher wind speeds, in which a few points outside of the general relationship can skew the binning method. We address this by removing bins clearly influenced by outliers. We also remove months of data that are contaminated by malfunctioning sensors or extraneous influences. For example, four stations near the $M_{\rm w}$ 6.4 Kaktovik earthquake and subsequent swarm show unrealistically elevated noise for August to December of 2018

(Fig. S9). We also removed 14 stations that never exhibited wind speeds in excess of 3 m/s and showed no correlation to seismic power (Fig. S10). We believe that the meteorological sensors at these sites were sheltered from the wind impacting ground motion or were functioning poorly. In total, 20 of the 130 stations with data for 2018 were removed for having suspect data or other sources of noise. Site-specific notes on cleaning the data can be found in the supplemental material (Text S2 and Table S3). In total, we compute the wind sensitivity for each month of 2018 for the 110 stations with data.

Patterns

The relationship between wind speed and seismic energy varies widely (Fig. 4). In general, wind-induced seismic noise is most prominent in the high-frequency bands (2, 6, and 18 Hz bands). The 0.1 Hz band is dominated globally by seismic noise from ocean swells (Peterson, 1993; McNamara and Buland, 2004). The impact of wind is present but is typically masked by the much larger influence of this microseism noise (Fig. 1). The majority of stations show no reliable wind sensitivity in the 0.1 Hz band, presumably because of this overprinting. For this reason, we do not include the 0.1 Hz band in subsequent analyses. The 0.02 Hz band is characterized by many high-noise points unrelated to wind. But unlike the 0.1 Hz band, the 0.02 Hz band sensitivity curves are robust enough to be interpretable. In general, the 0.02 Hz band has much lower wind sensitivity, with only 16 of the 110 stations having a wind sensitivity >1 dBs/m. In contrast, 61 of the 110 stations in the 6 Hz band have a sensitivity >1 dBs/m. We observe significant differences in critical wind speed, slope, and the roll off the curve at high wind speeds. In general, the critical wind speed occurs at low wind speeds (<4 m/s) for very sensitive stations and at high speeds (>8 m/s) for low-sensitivity stations.

CONTROLS ON WIND SENSITIVITY Geographic variation

Maps give a sense of the spatial distribution of wind sensitivity. Figure 5 highlights this for the 0.02 Hz and 6 Hz bands. In both the bands, the same six stations—I20K, H19K, H25L, G25K, H29M, and G29M—show very high sensitivity. These stations are in low-elevation forested basins, underlain by Cenozoic sedimentary basins (Wilson et al., 2015). The highest sensitivity stations at 0.02 Hz are in the 64° and 68° latitude bands, in the southwestern part of the state and Aleutians, as well as a couple of isolated cases. In the high frequencies (Fig. 5b), stations that are in mountains or hills tend to have lower sensitivity than stations in flat basins. However, this generalization does not hold true for all stations, and there are many examples of stations in very similar geographic locations with vastly different sensitivity values (e.g., I20K and H20K, Fig. 5a). We infer that wind sensitivity has no fundamental variation by region and is instead controlled almost entirely by the local surroundings.

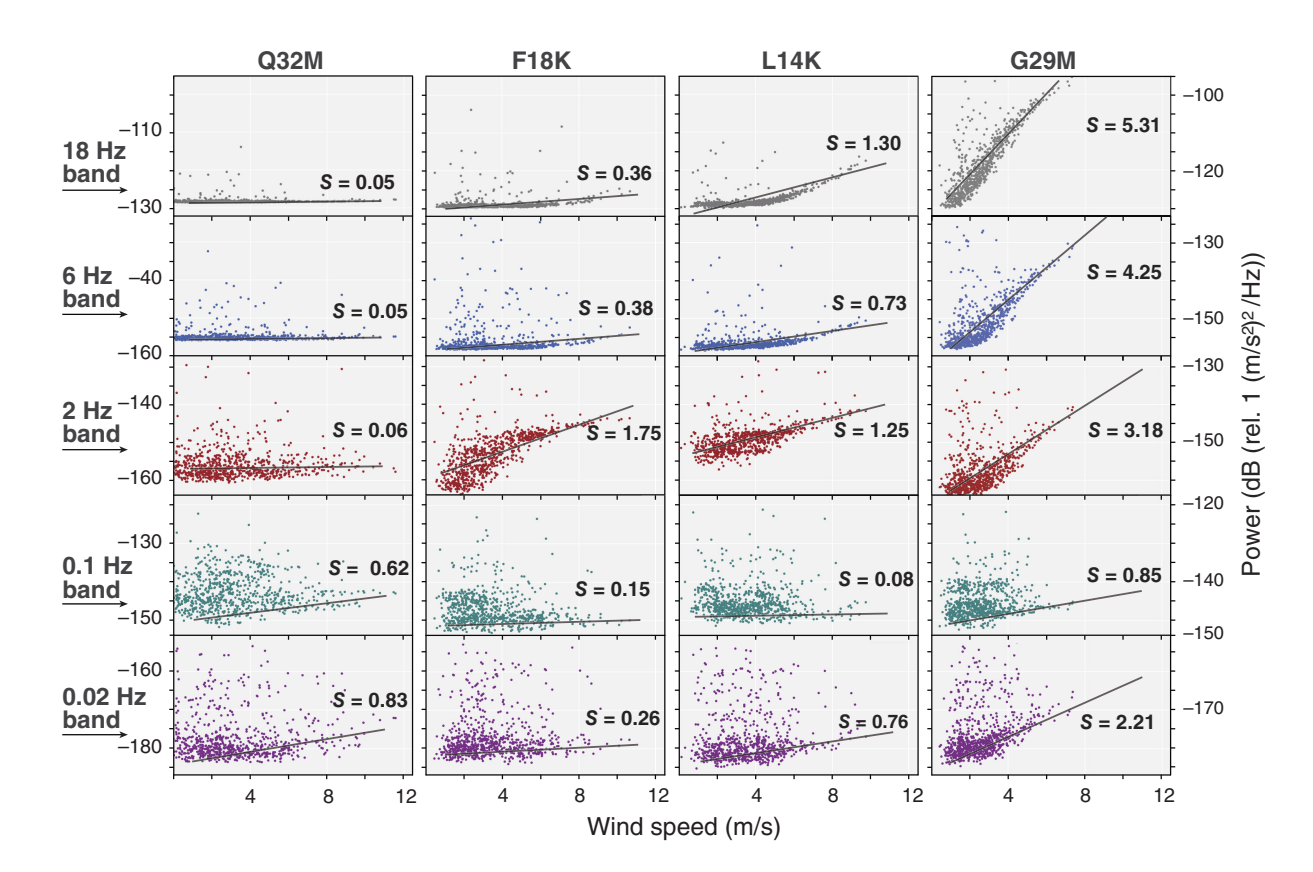


Figure 4. Examples of the wind–seismic relationship across frequencies and stations for July 2018. Labeled sensitivities are the slope of the fit. In general,

the 18 Hz band is the most responsive. The 0.1 Hz band is overprinted by strong noise sources, masking much of the specific relationship to wind.

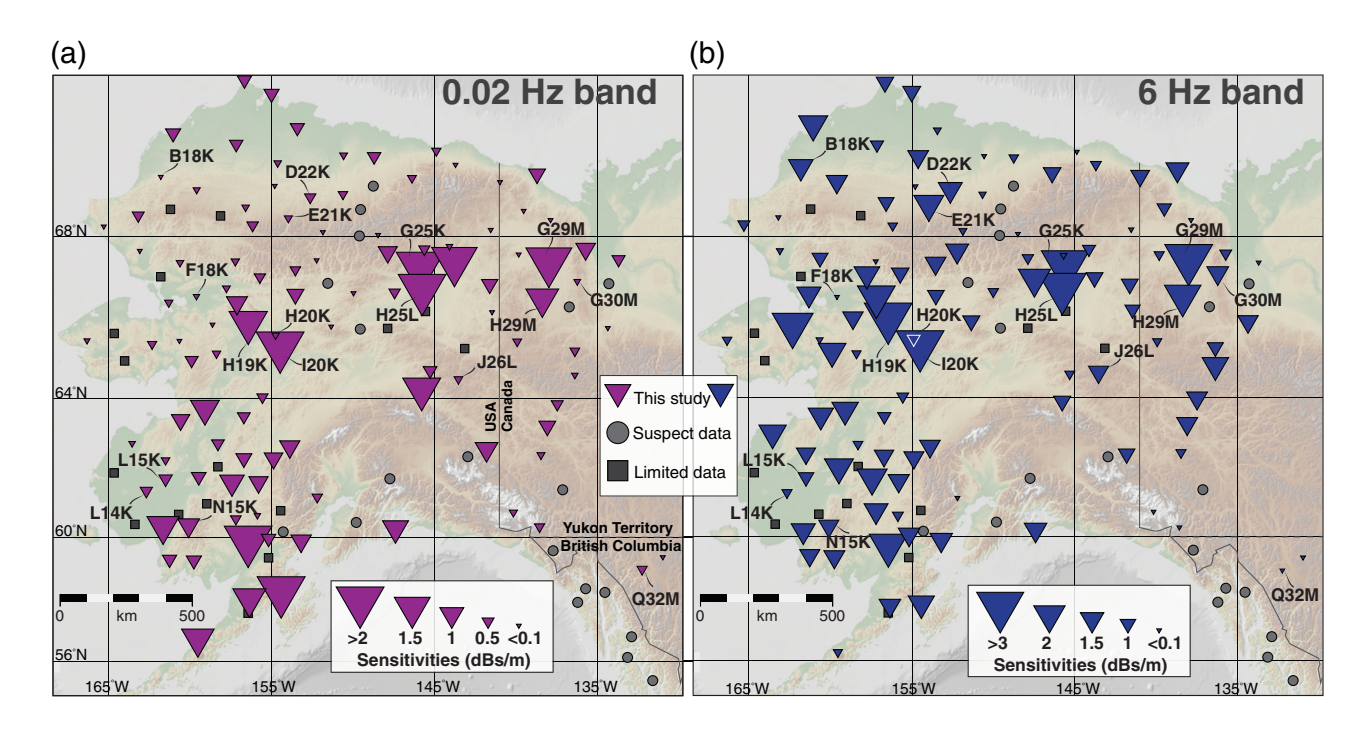


Figure 5. Map of Alaska and northwestern Canada showing Transportable Array (TA) network stations with colocated seismic and wind sensors (146 stations). (a) Geographic distribution of wind sensitivity values for 0.02 Hz. The size of the triangles corresponds to the sensitivity. Stations that have few wind speed points for the 2018 calendar year are labeled as dark gray

squares. Stations that have physically suspect data or other dominant sources of noise (i.e., rivers, cities, glaciers) are labeled as light gray circles. (b) Geographic distribution of wind sensitivity for the 6 Hz band. Stations A36M and C36M are outside of map bounds. We include labels for stations that are mentioned throughout the text.

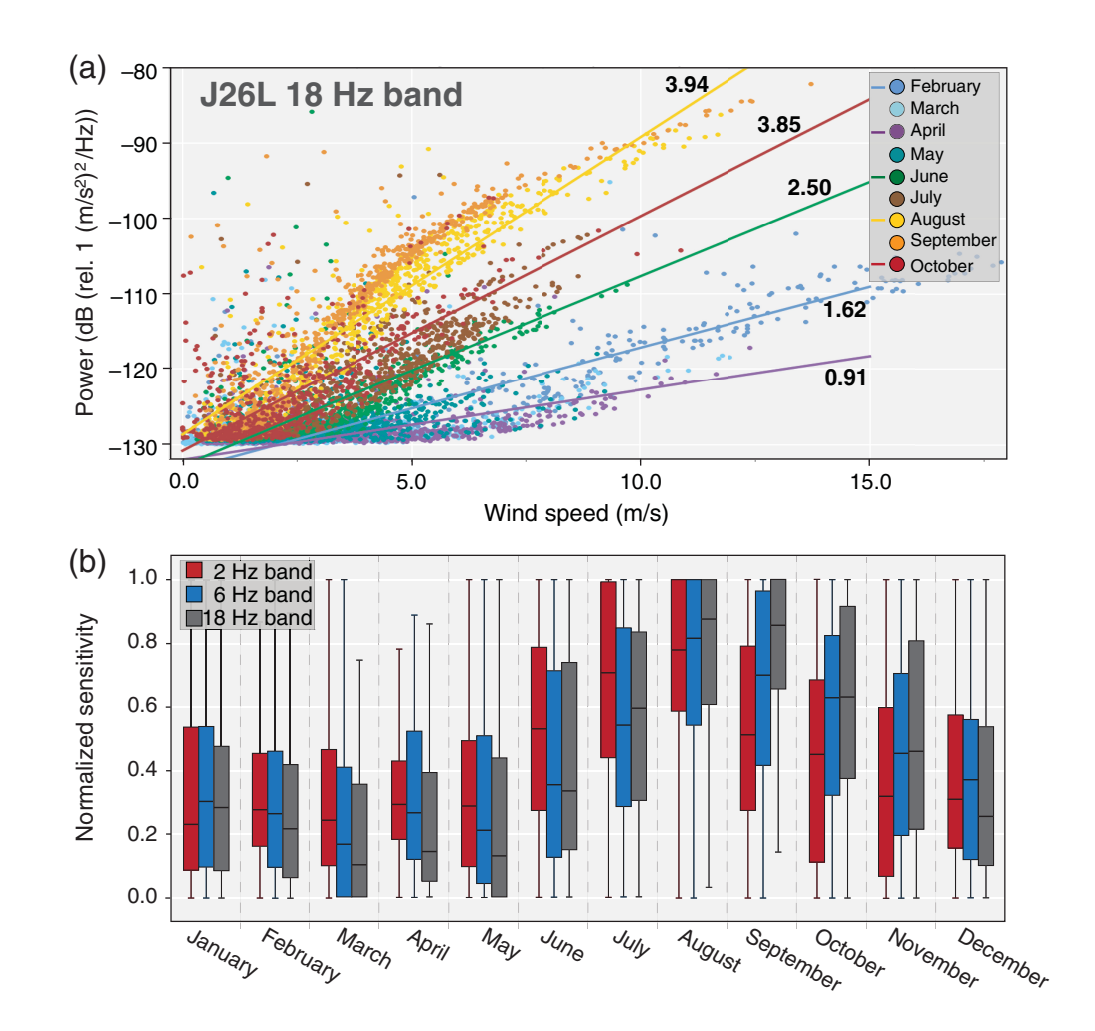


Figure 6. (a) Monthly wind speed and seismic power for station J26L at 18 Hz and corresponding wind sensitivity values. (b) Normalized monthly sensitivities for 2018 at 2 Hz. Boxplots extend from the lower to upper quartile values of the data, and whiskers extend to 1.5 times the interquartile range. The line within each plot is the median value. For clarity, outliers are not plotted.

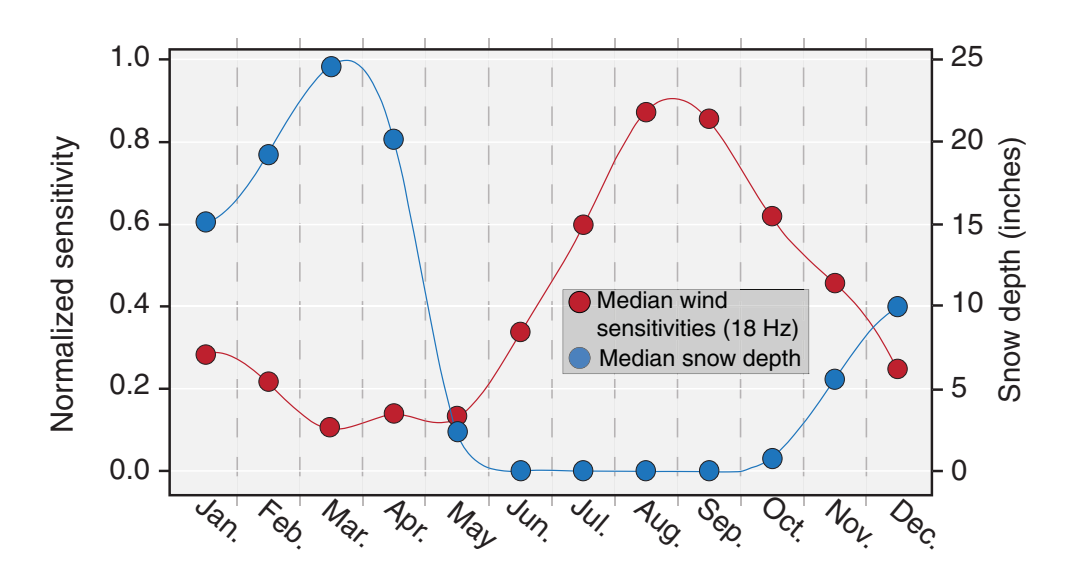


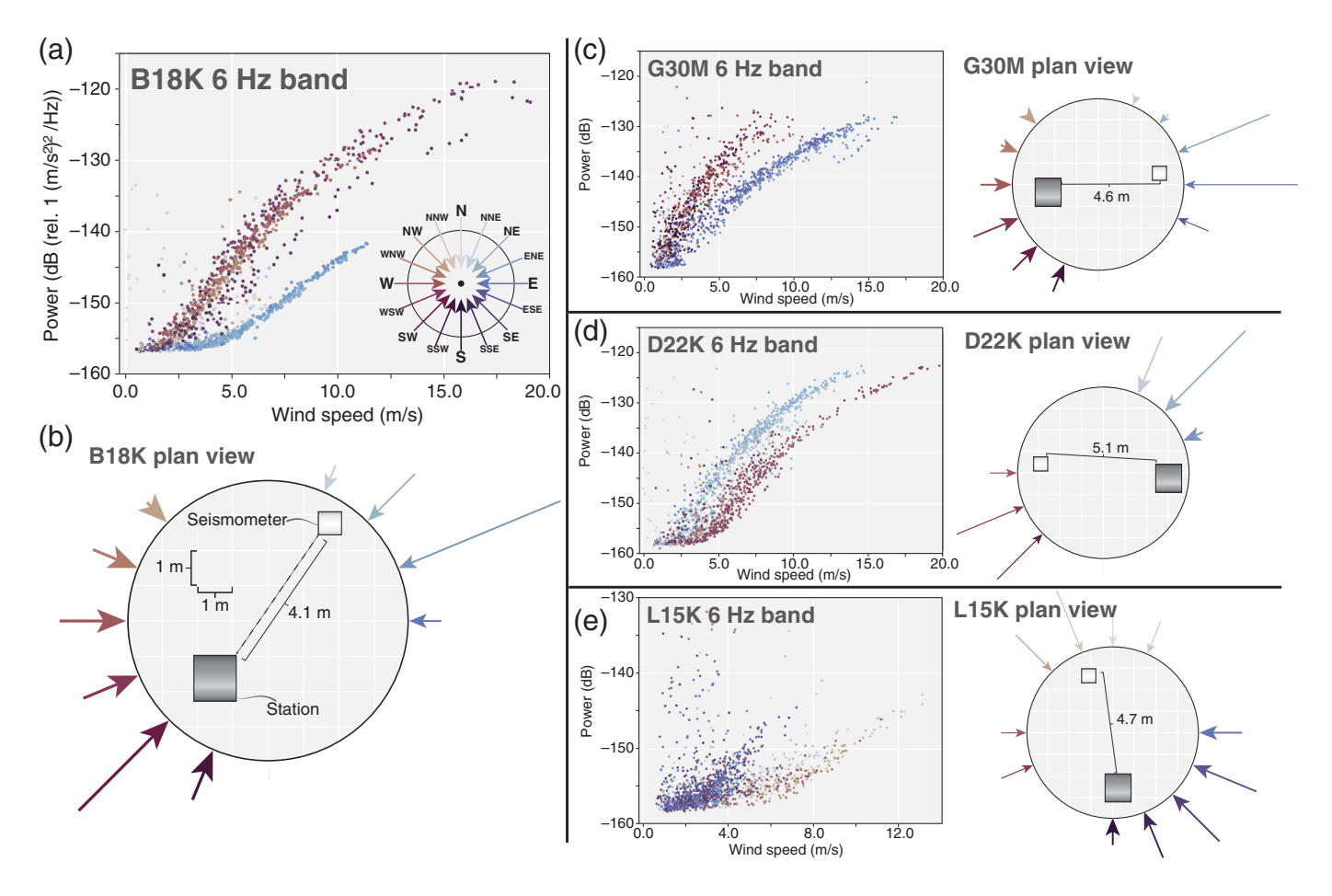
Figure 7. Monthly snow depth and normalized sensitivity. Average snow depth values are obtained from 54 snow stations in Alaska and the Yukon territory within close proximity (<60 km) of TA stations. The median of these values is shown in blue.

Seasonality

We use month-averaged sensitivities to identify seasonal patterns. Figure 6a provides an example for station J26L, where seismic energy in August and September can be 25 dB greater than in February, March, and May. The same amount of wind has a far larger influence in the late summer. Months with high sensitivity also show a lower critical wind speed (~0 to 2 m/s) than less sensitive months (5–6 m/s).

We compute the normalized sensitivities for each station so that patterns can be compared on the same scale. The normalized sensitivity at each station s_n is the monthly sensitivity s in relation to the months with the maximum sensitivity s_{max} and the minimum sensitivity s_{\min} , such that $s_n = \frac{s - s_{\min}}{s_{\max} - s_{\min}}$. This puts each station on a scale of 0-1. Stacking the normalized monthly sensitivities for all stations, we observe a cyclic pattern in the high frequency bands (2, 6, 18 Hz band; Fig. 6b). We observe a sinusoidal-like pattern with the maximum in August and the minimum in March. with a roughly threefold oscillation in sensitivity throughout the year. The 0.02 Hz band does not show as clear a trend, though in this band 70% of the stations still show their highest sensitivity in the four months of July to October, suggesting similar seasonal controls (Fig. S11). Of the 110 stations, 82 follow the general seasonality pattern in Figure 6b, with 79 stations having their maximum sensitivity during the months of July, August, September, and October (Table S3).

The seasonal pattern in sensitivity anticorrelates with snow depth (Fig. 7). We use monthly



average snow depth data for 2018 from 54 snow stations in Alaska and the Yukon Territory using the xmACIS2 database (Eggleston, 2021). We compute the median snow depth and compare it to the median normalized sensitivities (Fig. 7). Observe in Figure 7 that the least sensitive month, March, corresponds to the greatest snow depth in the network. The sensitivity decreases with an increase in snow depth and vice versa. Interestingly, sensitivity stays relatively low during the spring months (May, June, and July), when the snowpack is fully melted. To verify these patterns, we compare monthly sensitivities at 38 stations with seasonal patterns at 25 nearby snow stations and find similar trends (Fig. S12). We interpret these patterns as snow burying vegetation and other surface obstacles.

Wind direction

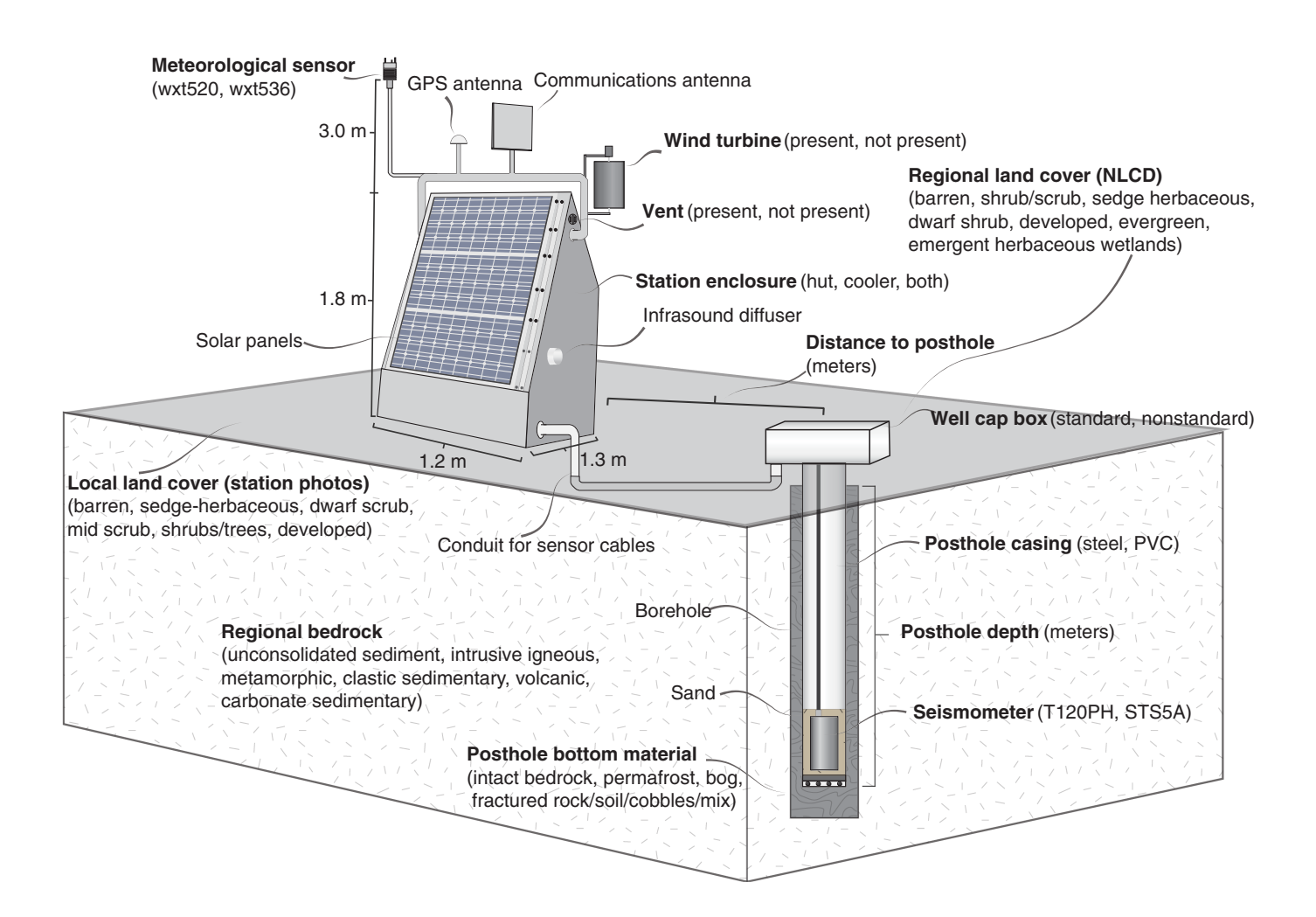
Although not networkwide or across all frequency bands, there are stations that show a substantial difference in sensitivity based on the wind direction (Fig. 8). In these examples, the amount of seismic energy can differ by tens of decibels depending on wind direction. This is primarily observed in the 2, 6, and 18 Hz bands. We examine eight stations that exhibit the strongest directionality. After investigating site photographs, we find that all the eight stations share the same arrangement of the seismometer borehole with the hut. In all examples, the sensitivity is higher when wind contacts the station hut before the borehole. The clearest explanation is that the hut itself

Figure 8. (a) Wind speed versus seismic power for station B18K during June and July 2018. The color represents the wind direction as labeled on the rose diagram. (b) Plan view of the station hut in relation to the seismometer borehole and predominant wind directions. Vectors indicate wind direction, with the length corresponding to the number of observations and the thickness representing sensitivity. The position of the hut and borehole was inferred from station photos and measurements from Busby and Aderhold (2020). Panels (c,d,e) show the same analysis for stations G30M, D22K, and L15K, respectively.

creates downwind turbulence, which then couples into the ground, potentially through interaction with the borehole cap. The stations that show the clearest directionality—B18K, D22K, and G30M—have little to no vegetation, furthering the suggestion that the hut creates most of the turbulent air.

Environmental factors and site conditions

There are numerous external datasets that make statistical comparison to environmental factors possible, including land cover datasets, geologic maps, and station photos to provide information on local vegetation, regional vegetation, the presence of trees, material in boreholes, remoteness classification, bedrock type, elevation, distance to moving water, distance to standing water, and distance to the ocean. We use station metadata and installation reports (Busby and Aderhold, 2020) to assess site design factors such as proximity of buildings, type of enclosure,



posthole casing, posthole depth, distance from posthole to hut, type of instrumentation, and the presence or absence of a wind turbine, vent, or wind deflector. Figure 9 illustrates a typical Alaska TA station and the parameters investigated here. A full description of the environmental, and site-specific parameters and the data sources can be found in Table S4.

We use single and multivariable least-squares linear regression to assess the significance of these factors in controlling wind sensitivity. We use the full-year sensitivity values. Some of the influencing factors are inherently numerical (e.g., elevation). For categorical variables, individual linear regressions are taken between each variable, and are assessed by the multivariate R^2 and p-value. The regression p-value and coefficient of determination R^2 provide a sense of statistical significance and whether the null hypothesis can be rejected (p < 0.05). These measures are possible when the dataset is sufficiently large. We supplement this with a number of anecdotal observations when the influence on sensitivity seems notably compelling, even at a small number of stations.

Land cover. We use the Alaska NLCD (Dewitz, 2021) to identify eight land cover types spanned by our stations (Fig. S13). For the categories of grassland, evergreen, and wetlands, we have just a couple of stations, and the database does not

Figure 9. Schematic of typical TA station. Bold labels represent parameters that are included in the statistical analysis, with the different variable options in parentheses. Unit of measure is given if numeric and more than one option is given if categorical. Diagram (not to scale) modified from Busby and Aderhold (2020).

cover the 22 stations in Canada. To resolve these issues, we use station photos together with the NLCD categorizations to subset 110 stations into six categories: barren, dwarf scrub, sedge-herbaceous, mid-scrub, shrubs and trees, and developed (Text S3). This categorization emphasizes vegetation height within \sim 20 m of the station.

Vegetation has a strong control on wind-induced seismic noise (Fig. 10a). Barren and dwarf scrub regions have consistently low wind sensitivity values (~0.5 dB/(m/s) at the 18 Hz band), whereas stations with bushes and trees have considerably higher wind sensitivities (~2.4 dB/(m/s) at the 18 Hz band). Further inspection of Figure 10a illustrates that wind sensitivity is not controlled as much by vegetation type but by the height of the vegetation: the mid-scrub and sedge/herbaceous categories have very similar sensitivities, consistent with their similar heights. The most sensitive and least sensitive stations follow this general trend (Tables S5 and S6). A similar result is found by regressing sensitivity against the simple binary

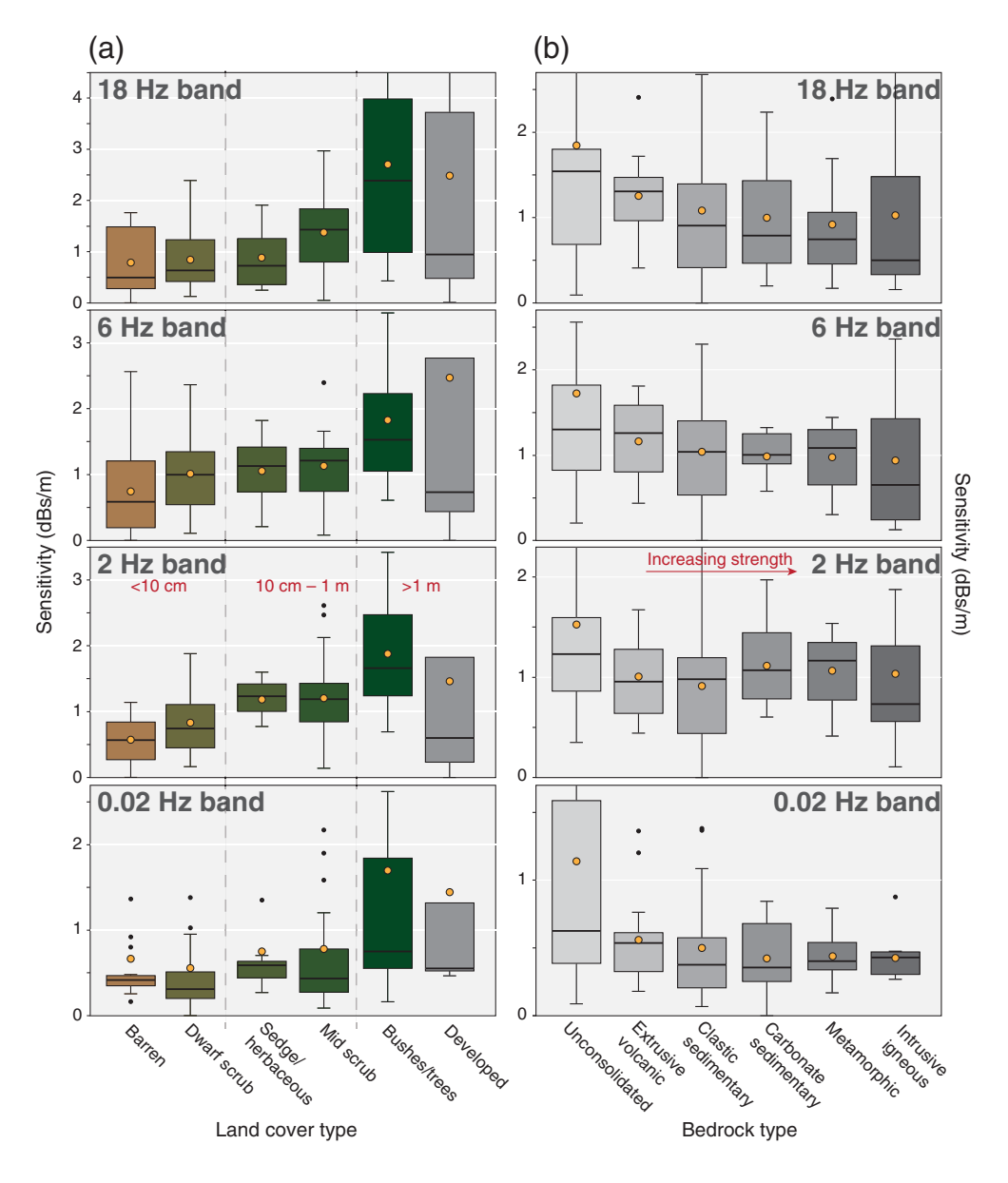


Figure 10. (a) Wind sensitivity for 2018 binned by land cover type at 0.02, 2, 6, and 18 Hz bands. Boxplots extend from the lower to upper quartile values of the data, and whiskers extend to 1.5 times the interquartile range. The line within each plot is the median value for the monthly sensitivity. Orange circles are mean values. Outliers are plotted as black dots. (b) Bedrock categorization versus wind sensitivity. Rock types are in order of relative strength, with the weakest rocks on the left and the strongest rocks on the right.

presence or absence of trees (Fig. S14; Busby and Aderhold, 2020). The best explanation is that taller vegetation provides more coupling to the wind, which results in increased ground motion. Taller vegetation presents more surface area to the wind and also provides a larger "lever arm" to the ground. It is interesting that the patterns observed here are opposite of what is observed in infrasound data analyzed over the same network (MacPherson *et al.*, 2022). Although vegetation can increase seismic noise, it can shield infrasound from wind influences.

Bedrock and posthole conditions. We use two parameters to look at the influence of bedrock and near-surface material.

We use the Alaska State Geological Map (Wilson *et al.*, 2015) and Yukon Geologic Map (Yukon Geological Survey, 2022) to assign each station to one of six rock types (Fig. 10b). We also use the four categories of borehole material identified during site installation (Busby and Aderhold, 2020).

The rock type in the substrate appears to have some control over wind sensitivity. In general, stations that are in unconsolidated sediment have much higher sensitivity, whereas stations in stiff rock (igneous and metamorphic) have lower sensitivity (Fig. 10b). In the high frequency band (especially the 6 and 18 Hz bands), sensitivity values tend to decrease with an increase in rock strength. Although the median values show this trend, there is obvious variation indicated by the quartiles and whisker plots in Figure 10. This trend is intuitive. Stronger rocks are less susceptible to strain when subjected to the same surface stresses. Though we observe some geographic correlation with sedimentary basins, not unlike prior highnoise observations (Tape et al., 2017; Smith and Tape, 2019), we propose that the high sensitivity to wind (not to be confused by high overall noise) is governed directly by softer rock,

which happens to be common in basin environments.

Comparing the posthole material and sensitivities, there are few clear trends (Fig. S15). However, stations that are built in bogs have very high sensitivities. Although limited to only a few stations and not surprising, this suggests that bogs amplify wind noise, undoubtedly due to the low cohesion and soil strength.

Other station parameters. Several other parameters show statistically interesting trends that should be treated with caution due to the likelihood of covariance. Stations with wind turbines somewhat surprisingly show a slight negative

correlation with sensitivity (Fig. S16). However, we observe that many wind turbine stations are on the north slope, where there are no trees or high vegetation—conditions strongly associated with low sensitivity. Elevation has a slightly negative correlation with sensitivity (Fig. S17), which likely reflects the lack of vegetation at high elevations. A station's distance from the ocean has a slightly positive correlation (Fig. S18), which we propose is due to the general increase in vegetation height moving away from the ocean. Stations near buildings tend to have high sensitivities, supporting previous observations of wind coupling with structures (Fig. S19; Johnson et al., 2019). One unexpected parameter to show significance is the posthole casing material. Stations with polyvinyl chloride (PVC) casing tend to have much higher sensitivities than stations with steel casing (Fig. S20). Although the PVC category is limited to 11 stations, four of the stations are within the top 7% percentile of sensitivities. Table S7 shows all statistically significant variables.

DISCUSSION

The colocation of wind and seismic sensors in Alaska provides an unparalleled opportunity to quantify effects on ground-motion energy. We find a first-order relationship, in keeping with prior studies (Dybing *et al.*, 2019; Lott *et al.*, 2017; Johnson *et al.*, 2019). Though we observe higher-order features at times (critical wind speed, roll off at high speeds), we do not find these to be sufficiently widespread to allow statistically meaningful conclusions (Fig. 3b).

The height of surrounding vegetation is one of the strongest controls (Fig. 10a). This is intuitive, as taller vegetation provides more opportunity for wind to couple to the ground. We find a second, less intuitive connection as well. A small number of stations with tall vegetation demonstrate extremely high sensitivity, accompanied by a suspicious absence of strong wind. We theorize that these observations are biased, because the vegetation is sufficiently tall that it shields the anemometer from the true wind speed. Strong wind will continue to couple into the ground and cause elevated seismic energies, but be recorded as having artificially low wind speeds. We believe this effect explains the suspicious absence of strong wind at stations where regional meteorology would suggest otherwise (Fig. S7). This mechanism is supported by observations such as P29M that exhibit this shielding effect only during the summer months when surrounded by tall shrubby vegetation (Fig. S21).

The anticorrelation between rock strength and wind sensitivity is also intuitive, because weaker rock allows more ground motion when subjected to the same force. Some caution is warranted, however, because of the correlations between rock type, vegetation, and geologic setting. Many stations surrounded by bushes or trees are located in unconsolidated materials. Also, unconsolidated materials are more common in settings in which other factors, such as basin amplification (Tape *et al.*, 2017), are likely to influence the data. For these reasons, the

rock type pattern in Figure 10b is likely not entirely separable from vegetation and geologic setting. These mechanisms are also presumably frequency dependent.

We examine a range of frequency bands to understand how wind can impact different types of seismic analysis. We also examine different frequencies, because the mechanisms that couple the atmosphere to the ground are known to be frequency dependent. Considerable research has been devoted to atmospheric coupling at frequencies below the microseism band (e.g., Ziolkowski, 1973; Zürn et al., 2007; De Angelis and Bodin, 2012). These studies demonstrate how variations in barometric pressure influence seismic records, primarily by inducing tilt in the near surface. Zürn et al. (2007) present two models for using barometric pressure to remove seismic noise from horizontal component seismograms at long periods. They find dramatic variance reductions at times, whereas other times they find little reduction at all. Although barometric pressure and wind are not the same, they are highly interrelated. Wind gusts create barometric pressure changes over short distances. Over longer distances, barometric pressure drives the wind. In raw records, we observe visual correlations between strong gusty wind and barometric pressure on scales of several seconds to minutes (Fig. S22). Turbulence caused by interaction with the ground and vegetation seems unlikely to create ground motion at periods of several tens of seconds, such as our 0.02 Hz band. However, wind speed has strong oscillations on these scales. We experience these as gusts. The barometric pressure changes caused by these wind variations are the more likely source of ground motion. This is confirmed by the fact that only the 0.02 Hz band shows notably higher sensitivity on the horizontal components—in keeping with prior observation of barometric pressure at long periods (Figs. S1-S3). Theoretically, a strong but constant wind would not drive this mechanism. In practice, however, we find few episodes of strong wind that do not vary on the scale of seconds to minutes.

Wind sensitivity at frequencies above the microseismic band compromises local and regional earthquake analysis. *P* and *S* phase arrivals for most earthquakes are rich in these frequencies, especially the 2 and 6 Hz bands. Wind compromises seismic detection and monitoring as well as analysis techniques that rely on these phases, such as receiver functions, body wave tomography, and first-motion focal mechanisms. Understanding the role of wind may not fully mitigate these effects, but it can at least help forecast where and when monitoring systems may be compromised.

We find a widespread anticorrelation between snow depth and seismic noise (Fig. 7). This pattern is most striking at high frequencies, though we observe evidence for it even in the 0.02 Hz band. Several factors may contribute to this. Snow buries vegetation and surface obstacles, creating a smooth surface that can reduce the ability for wind to couple into the ground. Snow has also been shown to dampen infrasound in the

frequency ranges examined here (Macpherson et al., 2022). We presume this influence could similarly reduce the influence of turbulent air on ground motions. We cannot preclude the role of frozen ground as well. Across much of this network, the top meter or more of soil freezes in the winter. This increased rigidity can reduce the motion of the ground. Interestingly, we observe a lag between the disappearance of spring snow and heightened wind sensitivity. We attribute this to the delay in vegetation growth once snow has melted, though the slow thawing of frozen ground could explain this lag as well.

We find a small number of stations located in low vegetation areas that are strongly influenced by wind direction (Fig. 8). The directionality strongly supports the conclusion that ground motion is generated by turbulent wind after interacting with the hut upstream of the borehole. The effect is likely amplified by the borehole cap that protrudes above the surface. We postulate that directionality is not observed networkwide, because most stations have some vegetation nearby, which creates turbulent air from all wind directions. Interestingly, six of these stations (B18K, D22K, F17K, G30M, J30M, and L15K) show much stronger wind direction dependence in the spring and summer months (April to September). Although this sample size is small, it fits our turbulence and borehole cap hypotheses. The presence of significant snow buries the exposed borehole, insulating it from the turbulent air.

We demonstrate several considerations for future site placement. Land cover models, geologic maps, and wind speed data can be used to estimate in advance the amount of noise at a station. In practice, the siting of new seismic stations includes considerations not listed here, such as telemetry, helicopter access, and solar power. As feasible, however, stations will experience less wind noise in locations with limited vegetation, competent rock, and steel posthole casings. In addition, our directional analysis suggests that placing the seismometer on the windward side of the station may reduce noise. And although snow can create power and telemetry complications for station operations, it is worth appreciating the significant role it can play in reducing wind noise. In our opinion, the apparent noise damping provided by snow is substantial enough to warrant a dedicated investigation in the future.

Looking forward, we should anticipate new patterns in wind noise, because the changing climate affects vegetation, snow depth, ground temperatures, and weather patterns. The world's northern latitudes are evolving rapidly due to changes in climate (Chapin *et al.*, 2005), with Alaska warming more than twice as fast as the rest of the United States (Stewart *et al.*, 2013). Aerial photography, remote sensing, ecological monitoring, and dendrochronology have documented widespread shrub expansion in Arctic and alpine regions (Tape *et al.*, 2006; Myers-Smith *et al.*, 2011). We expect wind sensitivity to increase at stations that transition from herbaceous plants and grasses to taller shrubs, with an expected two- to threefold

increase in wind sensitivity and decreased critical wind speed. The annual snowfall in Alaska is expected to decrease in the coming century, especially at elevations below <1000 m (Lader et al., 2019). In addition, the length of the snow season has decreased in recent decades—a pattern expected to continue (Stewart et al., 2013). Wind sensitivity will track changes in snowfall, especially changes in the onset and melting of snowpacks. This will negate some of the quieting effects that we currently benefit from in the winter months. Wind speed and storms are also expected to change under current climate models (Redilla et al., 2019). Notably, the average wind speed is expected to increase during the winter and decrease during the summer. Furthermore, models suggest that there will be increased numbers of extreme weather events (Poujol et al., 2020; Bachand and Walsh, 2022). Changes in the average wind speed will likely have little effect on station sensitivity unless the maximum wind speeds experienced are close to the critical wind speed. Although these forecasts would not increase wind sensitivity directly, they do point to the potential for higher wind noise in general. These higher overall wind speeds, further compounded by the increases in wind sensitivity, point to a future in which wind-generated seismic noise is appreciably elevated over today's levels.

DATA AND RESOURCES

The facilities of Incorporated Research Institutions for Seismology (IRIS) Data Services, and specifically the IRIS Data Management Center, were used to access waveforms, related metadata, and/or derived products used in this study. IRIS Data Services are funded through the Seismological Facilities for the Advancement of Geoscience (SAGE) Award of the National Science Foundation under Cooperative Support Agreement EAR-1851048. Seismic and wind data were accessed through IRIS Web Services (https://service.iris .edu/, last accessed September 2023), including the Transportable Array (TA) network (IRIS Transportable Array, 2003) and the AK network (Alaska Earthquake Center, University of Alaska Fairbanks, 1987). The supplemental material includes datasheets (.xlsx, .csv) that comprise sensitivity values for the frequency bands investigated and station parameters used in the statistical analysis, and a document (.pdf) that contains descriptions, tables, and figures that provide more context to the concepts and results discussed in the main article.

DECLARATION OF COMPETING INTERESTS

The authors acknowledge that there are no conflicts of interest recorded.

ACKNOWLEDGMENTS

The authors acknowledge the Alaska and Canada native nations upon whose land our study area resides. This research was performed under support from the National Science Foundation Award OPP-2024208, the Colorado College Noblett-Witter Family Fund, and the Hannigan Family Fund. Data from the Transportable Array (TA) network were part of the EarthScope USArray facility operated under National Science Foundation (NSF) Cooperative Agreement EAR-1261681. Data from the AK network are supported by the U.S. Geological

Survey (USGS) Advanced National Seismic System (ANSS) program Cooperative Agreement Number G22AC00001 and the Alaska Office of the State Seismologist. The authors thank Adam Ringler at the Albuquerque Seismological Laboratory for insightful comments that greatly improved the final article and for sharing data for the power spectral density (PPSD) comparison. The authors also thank Christine Siddoway and Kasey Aderhold for insightful conversations and input, and Daniel Lewinsohn for contributions in developing the statistical analysis.

REFERENCES

- Aderhold, K., K. E. Anderson, A. M. Reusch, M. C. Pfeifer, R. C. Aster, and T. Parker (2015). Data quality of collocated portable broadband seismometers using direct burial and vault emplacement, *Bull. Seismol. Soc. Am.* 105, no. 5, 2420–2432, doi: 10.1785/0120140352.
- Alaska Earthquake Center, University of Alaska Fairbanks (1987). Alaska regional network, *International Federation of Digital Seismograph Networks*, doi: 10.7914/SN/AK.
- Anthony, R. E., A. T. Ringler, and D. C. Wilson (2022). Seismic background noise levels across the continental United States from USArray Transportable Array: The influence of geology and geography, *Bull. Seismol. Soc. Am.* 112, no. 2, 646–668, doi: 10.1785/0120210176.
- Anthony, R. E., A. T. Ringler, D. C. Wilson, M. Bahavar, and K. D. Koper (2020). How processing methodologies can distort and bias power spectral density estimates of seismic background noise, *Seismol. Res. Lett.* **91,** 1694–1706, doi: 10.1785/0220190212.
- Bachand, C. L., and J. E. Walsh (2022). Extreme precipitation events in Alaska: Historical trends and projected changes, *Atmosphere* **13**, 388, doi: 10.3390/atmos13030388.
- Beauduin, R., P. Lognonné, J. P. Montagner, S. Cacho, J. F. Karczewski, and M. Morand (1996). The effect of the atmospheric pressure changes on seismic signals or how to improve the quality of a station, *Bull. Seismol. Soc. Am.* **86**, no. 6, 1760–1769, doi: 10.1785/BSSA0860061760.
- Busby, R. W., and K. Aderhold (2020). The Alaska Transportable Array: As built, *Seismol. Res. Lett.* **91,** no. 6, 3017–3027, doi: 10.1785/02202000154.
- Busby, R W., R. L. Woodward, K. A. Hafner, F. L. Vernon, and A. M. Frassetto (2018). The design and implementation of EarthScope's USArray Transportable Array in the conterminous United States and southern Canada, doi: 10.5281/zenodo.3758247.
- Casey, R., M. E. Templeton, G. Sharer, L. Keyson, B. R. Weertman, and T. Ahern (2018). Assuring the quality of IRIS data with MUSTANG, Seismol. Res. Lett. 89, no. 2A, 630–639, doi: 10.1785/0220170191.
- Chapin, F. S., M. Sturm, M. C. Serreze, J. P. McFadden, J. R. Key, A. H. Lloyd, A. D. McGuire, T. S. Rupp, A. H. Lynch, J. P. Schimel, *et al.* (2005). Role of land-surface changes in arctic summer warming, *Science* **310**, 657–660, doi: 10.1126/science.1117368.
- De Angelis, S., and P. Bodin (2012). Watching the wind: Seismic data contamination at long periods due to atmospheric pressure-field-induced tilting, *Bull. Seismol. Soc. Am.* **102**, no. 3, 1255–1265, doi: 10.1785/0120110186.
- Dewitz, J. (2021). National Land Cover Database (NLCD) 2019 products, doi: 10.5066/P9KZCM54.
- Dybing, S. N., A. T. Ringler, D. C. Wilson, and R. E. Anthony (2019). Characteristics and spatial variability of wind noise on near-

- surface broadband seismometers, *Bull. Seismol. Soc. Am.* **109**, no. 3, 1082–1098, doi: 10.1785/0120180227.
- Eggleston, K. L. (2021). xmACIS Version 1.0.66c, NOAA Northeast Regional Climate Center, NRCC, available at http://xmacis.rcc-acis.org/#.
- Frankinet, B., T. Lecocq, and T. Camelbeeck (2021). Wind-induced seismic noise at the Princess Elisabeth Antarctica Station, *Cryosphere* **15**, 5007–5016, doi: 10.5194/tc-15-5007-2021.
- Fyen, J. (1988). Diurnal and seasonal variations in the microseismic noise level observed at the NORESS array, *Phys. Earth Planet. In.* **63**, 252–268, doi: 10.1016/0031-9201(90)90026-T.
- Hutt, C. R., A. T. Ringler, and L. S. Gee (2017). Broadband seismic noise attenuation versus depth at the Albuquerque Seismological Laboratory, *Bull. Seismol. Soc. Am.* 107, no. 3, 1402–1212, doi: 10.1785/0120160187.
- IRIS Transportable Array (2003). USArray Transportable Array, International Federation of Digital Seismograph Networks, doi: 10.7914/SN/TA.
- Johnson, C. W., Y. Fu, and R. Bürgmann (2017). Stress models of the annual hydrospheric, atmospheric, thermal, and tidal loading cycles on California faults: Perturbation of background stress and changes in seismicity, *J. Geophys. Res.* 122, 10,605–10,625, doi: 10.1002/2017JB014778.
- Johnson, C. W., H. Meng, F. Vernon, and Y. Ben-Zion (2019). Characteristics of ground motion generated by wind interaction with trees, structures, and other surface obstacles, *J. Geophys. Res.* 124, 8519–8539, doi: 10.1029/2018JB017151.
- Lader, R., J. E. Walsh, U. S. Bhatt, and P. A. Bieniek (2019). Anticipated changes to the snow season in Alaska: Elevation dependency, timing and extremes, *Int. J. Climatol.* 40, 169–187, doi: 10.1002/joc.6201.
- Long, M. D., A. Levander, and P. M. Shearer (2014). An introduction to the special issue of earth and planetary science letters on USArray science, *Earth Planet. Sci. Lett.* **402**, 1–5, doi: 10.1016/j.epsl.2014.06.016.
- Lott, F. F., J. R. R. Ritter, M. Al-Qaryouti, and U. Corsmeier (2017). On the analysis of wind-induced noise in seismological recordings, *Pure Appl. Geophys.* 174, 1453–1470, doi: 10.1007/s00024-017-1477-2.
- Macpherson, K. A., J. R. Coffey, A. J. Witsil, D. Fee, S. Holtkamp, S. Dalton, H. McFarlin, and M. West (2022). Ambient infrasound noise, station performance, and their relation to land cover across Alaska, *Seismol. Res. Lett.* **93**, no. 4, 2239–2258, doi: 10.1785/0220210365.
- McNamara, D. E., and R. I. Boaz (2005). Seismic noise analysis system using power spectral density probability density functions—a stand-alone software package, available at https://pubs.usgs.gov/of/2005/1438/ (last accessed September 2023).
- McNamara, D. E., and R. P. Buland (2004). Ambient noise levels in the Continental United States, *Bull. Seismol. Soc. Am.* **94**, no. 4, 1517–1527, doi: 10.1785/012003001.
- Meltzer, A., R. Rudnick, P. Zeitler, A. Levander, G. Humphreys, K. Karlstrom, G. Ekström, R. Carlson, T. Dixon, M. Gurnis *et al.* (1999). USArray initiative, *GSA TODAY* **9**, no. 11, 8–10.
- Mohammadi, M., C. J. Hickey, R. Raspet, and V. Naderyan (2019). Wind-Induced ground motion: Dynamic model and nonuniform structure for ground, *J. Geophys. Res.* 124, 8478–8490, doi: 10.1029/2019JB017562.

- Myers-Smith, I. H., B. C. Forbes, M. Wilmking, M. Hallinger, T. Lantz, D. Blok, K. D. Tape, M. Macias-Fauria, U. Sass-Klaassen, E. Lévesque, et al. (2011). Shrub expansion in tundra ecosystems: dynamics, impacts and research priorities, Environ. Res. Lett. 6, 045509.
- Naderyan, V., C. J. Hickey, and R. Raspet (2016). Wind-induced ground motion, J. Geophys. Res. 121, 917–930, doi: 10.1002/2015JB012478.
- Nowacki, G. J., P. Spencer, M. Fleming, T. Brock, and T. Jorgenson (2003). Unified ecoregions of Alaska: 2001, doi: 10.3133/ofr2002297.
- Peterson, J. (1993). Observations and modeling of seismic background noise, U.S. Geol. Surv. Open File Rept. 93-322, doi: 10.3133/ofr93322.
- Poujol, B., A. F. Prein, and A. J. Newman (2020). Kilometer-scale modeling projects a tripling of Alaskan convective storms in future climate, *Clim. Dynam.* 55, 3543–3564.
- Quigley, C., M. West, S. John, S. Holtkamp, K. Aderhold, and A. Farrel (2021). Environmental influences on seismic noise across the U.S. Arctic, *AGU Fall Meeting*, AGU21-S55B-0136.
- Redilla, K., S. T. Pearl, P. A. Bieniek, and J. E. Walsh (2019). Wind climatology for Alaska: Historical and future, Atmos. Clim. Sci. 9, 683–702.
- Smith, K., and C. Tape (2019). Seismic noise in central Alaska and influences from rivers, wind, and sedimentary basins, *J. Geophys. Res.* **124**, 11,678–11,704, doi: 10.1029/2019JB017695.
- Stewart, B. C., K. E. Kunkel, L. E. Stevens, and L. Sun (2013). Part 7. Climate of Alaska in regional climate trends and scenarios for the U.S. national climate assessment, NOAA Technical Rept. NESDIS 142-7.
- Tanimoto, T., and J. Wang (2018). Low-frequency seismic noise characteristics from the analysis of co-located seismic and pressure data, *J. Geophys. Res.* **123**, 5853–5885, doi: 10.1029/2018JB015519.
- Tape, C., D. Christensen, M. M. Moore-Driskell, J. Sweet, and K. Smith (2017). Southern Alaska Lithosphere and Mantle Observation

- Network (SALMON): A seismic experiment covering the active arc by road, boat, plane, and helicopter, *Seismol. Res. Lett.* **88**, no. 4, 1185–1202, doi: 10.1785/0220160229.
- Tape, K., M. Sturm, and C. Racine (2006). The evidence for shrub expansion in northern Alaska and the Pan-Arctic, Global Change Biol. 12, 686–702, doi: 10.1111/j.1365-2486.2006.01128.x.
- Wilson, F. H., C. P. Hults, C. G. Mull, and S. M. Karl (2015). Geologic map of Alaska, doi: 10.3133/sim3340.
- Withers, M. M., R. C. Aster, C. J. Young, and E. P. Chael (1996). High-frequency analysis of seismic background noise as a function of wind speed and shallow depth, *Bull. Seismol. Soc. Am.* **86**, no. 5, 1507–1515, doi: 10.1785/BSSA0860051507.
- Yu, J., R. Raspet, J. Webster, and J. Abbott (2011). Wind noise measured at the ground surface, *J. Acoust. Soc. Am.* **129,** no. 2, 622–632, doi: 10.1121/1.3531809.
- Yukon Geological Survey (2022). Yukon digital bedrock geology, available at https://data.geology.gov.yk.ca/Compilation/3 (last accessed May 2023).
- Ziolkowski, A. (1973). Prediction and suppression of long-period non propagating seismic noise, *Bull. Seismol. Soc. Am.* **63**, no. 3, 937–958, doi: 10.1785/BSSA0630030937.
- Zürn, W., and E. Wielandt (2007). On the minimum of vertical seismic noise near 3 mHz, *Geophys. J. Int.* **168**, 647–658, doi: 10.1111/j.1365-246X.2006.03189.x.
- Zürn, W., J. Exß, H. Steffen, C. Kroner, T. Jahr, and M. Westerhaus (2007). On reduction of long-period horizontal seismic noise using local barometric pressure, *Geophys. J. Int.* 171, no. 2, 780–796, doi: 10.1111/j.1365-246X.2007.03553.x.

Manuscript received 9 May 2023 Published online 24 October 2023